Review of Scientific Instruments

Computational fluid dynamics analysis of char conversion in Sandia's pressurized entrained flow reactor

Cite as: Rev. Sci. Instrum. **91**, 074103 (2020); https://doi.org/10.1063/5.0005733
Submitted: 24 February 2020 . Accepted: 27 June 2020 . Published Online: 14 July 2020

Markus Bösenhofer, Ethan Hecht, Christopher R. Shaddix, Bernhard König, Johannes Rieger, and Michael Harasek

AIP Publishing

Review of Scientific Instruments ARTICLE scitation.org/journal/rsi

Computational fluid dynamics analysis of char conversion in Sandia's pressurized entrained flow reactor

Cite as: Rev. Sci. Instrum. 91, 074103 (2020); doi: 10.1063/5.0005733
Submitted: 24 February 2020 • Accepted: 27 June 2020 •
Published Online: 14 July 2020

Markus Bösenhofer,[1,2,a)] Ethan Hecht,[3] Christopher R. Shaddix,[3] Bernhard König,[2] Johannes Rieger,[2] and Michael Harasek[1]

AFFILIATIONS

[1]Technische Universität Wien, Institute of Chemical, Environmental and Bioscience Engineering, Getreidemarkt 9/166, 1060 Vienna, Austria
[2]K1-MET GmbH, Stahlstraße 14, Betriebsgebäude 88, 4020 Linz, Austria
[3]Combustion Research Facility, Sandia National Laboratories, Livermore, California 94550, USA

[a)]**Author to whom correspondence should be addressed:** markus.boesenhofer@tuwien.ac.at. **Tel.:** +43 1 58801 166251

ABSTRACT

Design and analysis of practical reactors utilizing solid feedstocks rely on reaction rate parameters that are typically generated in lab-scale reactors. Evaluation of the reaction rate information often relies on assumptions of uniform temperature, velocity, and species distributions in the reactor, *in lieu* of detailed measurements that provide local information. This assumption might be a source of substantial error, since reactor designs can impose significant inhomogeneities, leading to data misinterpretation. Spatially resolved reactor simulations help understand the key processes within the reactor and support the identification of severe variations of temperature, velocity, and species distributions. In this work, Sandia's pressurized entrained flow reactor is modeled to identify inhomogeneities in the reaction zone. Tracer particles are tracked through the reactor to estimate the residence times and burnout ratio of introduced coal char particles in gasifying environments. The results reveal a complex mixing environment for the cool gas and particles entering the reactor along the centerline and the main high-speed hot gas reactor flow. Furthermore, the computational fluid dynamics (CFD) results show that flow asymmetries are introduced through the use of a horizontal gas pre-heating section that connects to the vertical reactor tube. Computed particle temperatures and residence times in the reactor differ substantially from the idealized plug flow conditions typically evoked in interpreting experimental measurements. Furthermore, experimental measurements and CFD analysis of heat flow through porous refractory insulation suggest that for the investigated conditions (1350 °C, <20 atm), the thermal conductivity of the insulation does not increase substantially with increasing pressure.

I. INTRODUCTION

Sandia National Labs has a long history of conducting measurements on the ignition, combustion, and gasification of pulverized coal and biomass particles entrained into hot oxidizing gas at 1 atm, using a combination of optical measurements and extractive sampling.[1–9] A pressurized entrained flow reactor (PEFR) was developed at Sandia for extending these studies into pressurized combustion and gasification environments, due to the limited availability of high-quality data under these conditions.

Detailed information about temperature, pressure, and species distributions is necessary for extracting accurate chemical kinetic parameters from experimental measurements.[4,10–16] In many cases, spatially homogeneous temperature and species distributions are assumed for the model fitting procedure to simplify the regression methods. If strong heterogeneities exist in the reaction zone, these simplified assumptions can be a significant source of error and might produce misleading results. Using more sophisticated regression approaches reduces the introduced error but requires additional process information as well as computational effort.[15] Nonetheless,

in any case, having detailed knowledge of experimental equipment is a key to fully understand the investigated processes.

Computational fluid dynamics (CFD) has proven to be a vital tool for expanding the insight of existing equipment.[17–20] Therefore, in this study, detailed CFD simulation of the PEFR was performed to understand the internal reactor heat transfer and flow fields, followed by particle tracking through the PEFR's reaction zone. The reactive zone of the PEFR has previously been studied using CFD[21] by assuming wall temperatures suitable to predict the measured gas temperature profile. This is a common approach when modeling lab-scale equipment.[22–26] The approach presented in this work differs from the previously published CFD study, since besides the reactive zone, the pressurized vessel, the insulation layers, and the heating elements are considered in the simulation domain. As a result, the required boundary conditions are the convective and radiative heat transfer from the vessel to the surroundings and the surface temperatures of the heating elements. The wall temperature of the reactive zone is subject to local variations caused by the heat transfer within the cavities surrounding it. This approach captures temperature variations in the reaction zone and can help identify the cause (e.g., buoyancy-driven convection cells).

Measured surface and internal reactor temperatures were used to validate the simulation results. Although particle temperatures and gas phase temperatures can now be measured, no such data are currently available for model validation. A set of coal char gasification results was modeled to identify particle flow and conversion patterns in the PEFR using a non-coupled approach. In order to quantify the effect of a non-uniform temperature in the reaction zone, each experiment was also modeled with a uniform temperature profile. By comparing the results of the different temperature profiles, we examine the error introduced by assuming ideal reactor states when interpreting particle conversion experiments. Prior to the CFD analysis, a detailed reactor description is given in Sec. II.

II. PEFR DESIGN

Sandia's PEFR has been designed to study pressurized gasification and/or (oxy–fuel) combustion of solid fuels. The reactor design allows a maximum operation temperature of 1400 °C and maximum operation pressure of 20 atm. The PEFR can be operated under reducing or oxidizing conditions by using mixtures of carbon dioxide, carbon monoxide, hydrocarbon fuels, hydrogen, nitrogen, water vapor, and oxygen. In typical experiments, a dilute fuel particle stream (on the order of 1 g/min) is injected with nitrogen or carbon dioxide as a carrier gas from the top of the reactor. The main gas flow is preheated as it flows through a horizontal section. This unusual "L-shaped" reactor design allowed the reactor to fit within a single-story laboratory and also has the benefit of minimizing the length of the solid fuel injection line required to convey the solid fuel particle stream to the fuel injection point. A similar design has been previously developed at Brigham Young University.[27] Partially reacted fuel particles and combustion gases can be extracted via a water-cooled sampling probe at distinct axial reactor positions. Particles are rapidly quenched in the probe by nitrogen gas injection. The sample analysis procedure consisted of chemical analysis of the initial solid fuel sample and partially reacted solid particles that are removed from the flow exiting the sample probe by a hot cyclone with an approximate separation size cut of 15 μm. The ash-tracer method is used to determine the mean particle conversion.[24,28] Four-way optical ports exist at five discrete positions along the reactor although in the work described here, solid alumina rods blocked the ports to minimize flow disturbances along the reactor. Figure 1 depicts a schematic reactor representation of the reactor and indicates the locations where reactor temperatures and pressures are measured.

The reactor has two heating zones: the horizontal preheat zone and the vertical reactor zone. Each zone is controlled with proportional-integral-differential (PID) feedback from a thermocouple ($T_{C,preheat}$ and $T_{C,reactor}$), which is in contact with the SiC reactor tube at the positions shown in Fig. 1. An additional thermocouple is placed on the outside of the reactor tube at the location at which solid fuel particles are introduced into the main flow (T_1). Three thermocouples are also located along the outer skin of the pressure vessel. Thermal radiation dominates the heat transfer from the heating elements to the reactor surface within the cavities surrounding the SiC reactor.

The outer regions of the pressure vessel are filled with several concentric layers of solid, prefabricated refractory insulation composed of high-purity alumina or alumina–silica blends. The design of this reactor was based on previous experience at Sandia in designing and operating similar high-temperature furnaces as

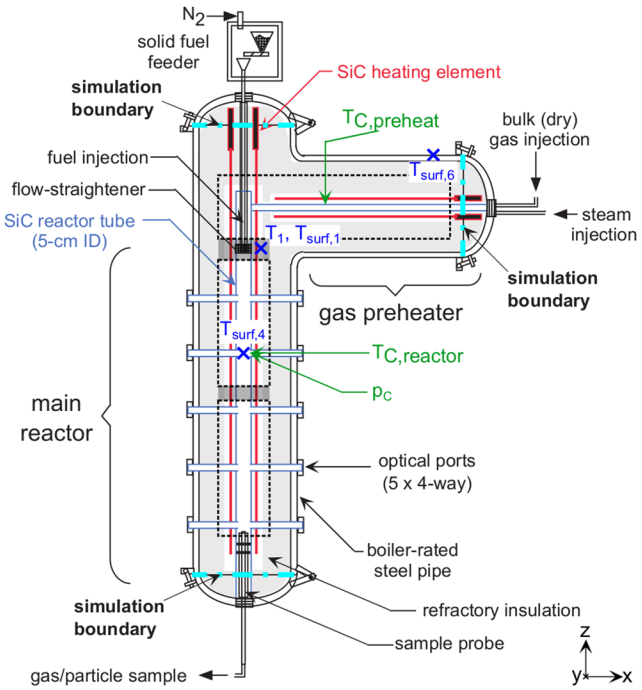

FIG. 1. Schematic reactor illustration. The dashed rectangles outline the heat transfer cavities, while the shading between the cavities represents the insulation "caps." Surface temperatures were measured at the steel pipe surface (T_{surf}), while the other temperatures were measured at the outer SiC reactor tube surface (T).

well as lessons learned from others in designing and operating similar pressurized reactors.[27,29–35] One common experience has been that heat losses from the reactors at high pressures have exceeded expectations and have often limited the operating envelope (p, T) of the constructed reactors. To better understand this phenomenon, a special insulation test vessel was constructed and used to investigate the insulation properties of high-temperature alumina-based insulation at elevated temperatures and pressures, as detailed in Appendix A of this paper. The results of this investigation confirmed the suspicion, expressed in some of these earlier publications, that buoyancy-driven convection cells are a major mechanism for the observed strongly enhanced heat loss at elevated pressures. To mitigate the impact of such convection cells, in the open space surrounding the vertical heating elements, horizontal insulation "caps" (discs of refractory material with minimal space between the refractory and the heating elements) were installed at two positions along the main vertical reactor at positions corresponding to "dead zones" in the radiant heating elements. This arrangement limited the vertical spaces in which convective cells would be able to freely move gas around the heating elements.

III. REACTOR SIMULATIONS

A. CFD reactor model

Measurements of the temperature distribution within the PEFR are limited to temperatures of the SiC reactor tube and surface temperatures of the pressurized steel pipe. This is insufficient to prove or disprove temperature and velocity uniformity. One approach to get a better understanding of the operational characteristics of the PEFR is to conduct a CFD study. Accurate predictions require proper knowledge of thermo-physical properties of the refractory materials as well as boundary conditions representing the correct physical situation. Available manufacturer's data for thermal conductivities of the refractory insulation materials are measured at 1 atm pressure. These refractory materials are highly porous, and their overall thermal conductivity is influenced by a complex interaction of conduction through the solid and gas phases, free convection of the gas in pores, and thermal radiation, with different mechanisms having relative dominance depending on the core material, its porosity and pore size distribution, and the relevant temperature and pressure.[36–38] In particular, while it is known that increased pressure increases the thermal conductivity, almost all reported studies have involved pressures of no more than 1 atm, so it is unclear how significant will be the changes in the thermal conductivity of the refractory material used in the PEFR over the investigated pressure range of 1 atm–8 atm.

To better understand the influence of elevated pressures on the thermal conductivity of the insulation materials, the materials were tested at elevated pressures in a more idealized geometry. A cylindrical vessel was pressurized with argon and heated to 1623 K at 1 atm and 20 atm pressures. Thermal heat-flux analysis has been applied to investigate thermal conductivities. These thermal conductivity experiments have been modeled prior to the full reactor setup to ensure the usage of reasonable thermo-physical properties in the reactor simulations. The results indicate that the changes in thermal conductivity of the employed refractory material are negligible at pressures up to 20 atm. Appendix A discusses these simulations in more detail.

Appendix B summarizes the employed polynomial expressions for the thermophysical properties of the solid refractories in the PEFR. The fluid properties are based on the NASA polynomials of the GRI3.0 mechanism.[39]

The CFD simulations employed the multi-region conjugated heat transfer solver *chtMultiRegionFoam*, which is part of the open-source CFD toolbox OpenFOAM®.[40] *chtMultiRegionFoam* couples multiple solid and fluid regions explicitly by sequentially solving for each region. This means that quantities of mixed (current and previous) time steps are taken for the coupling depending on the region sequence. This is referred to as loose coupling.[41] The solver supports thermal radiation and accounts for buoyancy effects in fluid phases. The fluid solver in *chtMultiRegionFoam* solves the Reynolds Averaged Navier–Stokes (RANS) equations and the sensible energy equation based on either internal energy or enthalpy using the SIMPLE algorithm. The k-ω-SST turbulence model[42] was used in the current study to account for the turbulent regions of the predominant laminar flow within the reactor. Radiation is modeled using the discrete ordinates method. Gas phase adsorption/emission is modeled by assuming gray mean absorption.[43] The solid solver solely solves for the sensible energy based on internal energy or enthalpy.

The simulation setup consists of multiple coupled solid and fluid zones (i.e., steel pipe, refractory material, SiC reactor, flow-straightener, fuel injection lance, lance insulation, probe insulation, cavities surrounding the reactor, and reactive fluid zone). Thermal coupling is accomplished by mixed boundary conditions, ensuring proper diffusive, convective, and radiative heat transfer between the regions. The fluid zones are assumed to be separate closed zones—thus, no pressure coupling is necessary.

The heating elements, coal lance, and quench are modeled as fixed temperature surfaces, and the reactor outer surface is subject to heat transfer by natural convection based on the surface temperature and vessel geometry.[44] The co-flow is introduced above the coal injection point from the side of the reactor sidearm at ambient temperatures at the desired flow rate and composition (coflowInlet), while coal or char particles are fed from the top at ambient temperatures with pure nitrogen (coalInlet). Nitrogen is introduced via the cooled sample probe to quench the reaction process. All particles and the fluid have to leave the reactor through the probe (probeOutlet). The boundary conditions are summarized in Table I. The Reynolds number of the gas flow in the reaction zone is ~1500 for both pressures.

The overall mesh consists of ~27 × 10^6 hexa-dominant cells. The central fluid region is discretized by 6.3 × 10^6 of these cells, which is ~20 times the resolution used in a previous CFD study of the same region.[21] A mesh study of the reactive zone was conducted using up to 40% coarser (2.45 × 10^6 cells) and up to 60% finer (29 × 10^6 cells) meshes. The results showed that mesh convergence was achieved for the mesh used for the reaction zone in the PEFR simulations. The loose region coupling required more than 300 000 iterations for the solution to converge. On 16 core AMD Epic 7351 with 16 GB RAM per core, this took between 14 days and 21 days.

The dilute coal/char mass flow (around 1 g/min or 1 ml/min on a volumetric basis) contributes ~0.5% and 10^{-4}% to the overall mass

TABLE I. Overview of boundary conditions for reactor simulations.

Surface	Boundary condition
SiC reactor tube	Mixed coupled
Refractory/insulation	Mixed coupled
Probe	Mixed coupled
Steel pipe	Mixed coupled
Fuel injection lance	T = 373 K
coalInlet	T = 300 K, 1 slpm N_2
coflowInlet	T = 300 K, 100 slpm CO_2
Quench	T = 373 K, 40 slpm N_2
probeOutlet	p = 1 atm/8 atm
probeOutlet	p = 1 atm/8 atm

flow and volumetric flow rates. The energy required to heat up the char particles and gasify them equals ~5% of the energy introduced by the co-flow. The CO emerging due to CO_2 char gasification contributes ~5% to the species composition at complete char burnout. Therefore, we neglect the char stream in the reactor simulations. Rather, the char conversion behavior is studied in a post-processing step after obtaining steady-state reactor gas-flow and temperature conditions. The quality of the reactor simulations is assessed by comparing temperature measurements and predictions for the two different pressure levels (1 atm and 8 atm) for which char conversion measurements were made. However, the local (on a cell basis) source terms of the char mass flow are higher than the global one. In the vicinity of the tip of the lance, the source terms (per second) for momentum, energy, and CO equal up to ~100%, 50%, and 15% of the amount in the corresponding cell. Individual cells in this region exceed these values. Source terms of similar scale occur in the quench region. Furthermore, the particle energy source/sink exceeds 10% in densely populated regions with local maxima of 45%–50%. However, the influence of the local source terms on the simulation results depends on the residence time of the fluid in the individual cells. For long residence times and high local source terms, the two-way coupled solution will deviate significantly from the one-way coupled approach presented here. Expected velocities and cell size suggest cell residence times well below one second. Nevertheless, comparing both approaches is necessary to investigate the error introduced by the one-way coupling.

Two distinct cases are examined for each pressure level: the simulated temperature distribution and an idealized, uniform temperature. The steady-state temperature distribution of the reactor simulation is taken for the first case, while a uniform reaction zone temperature of 1400 °C is taken for the latter, as this is the reactor wall set-point temperature for the experiments. Both temperature cases feature the same simulated velocity field.

Particle temperatures and char burnout are compared to identify the errors introduced by the homogeneity assumption. Furthermore, the particle pathways in the reactive zone are investigated.

B. Discrete particle gasification model

The particle conversion strongly depends on the gas temperature and composition near the particle surface. Therefore, the particle's pathway through the reaction zone is crucial if temperature and concentration gradients exist. In order to determine the actual coal/char conversion conditions, i.e., residence time, temperature, and CO_2 distribution, an uncoupled Lagrangian approach is used.

The coal/char conversion model uses pressure, velocity, species, and temperature fields from the steady-state reactor simulations and projects coal particles along the flow field. Particle and carrier gas properties are mapped for discrete intervals based on velocity and residence time to obtain heating rates and particle burnout.

The char conversion model uses a Lagrangian discrete particle approach with frozen carrier phase fields. The momentum, enthalpy, and species conservation equations of the Lagrangian particles are as follows:

$$m_P \frac{d\vec{u_p}}{dt} = \vec{F_d} + \vec{F_g} = \frac{\pi d_P^2}{8} c_D \rho_g |\vec{u_p} - \vec{u_g}| (\vec{u_p} - \vec{u_g}) + m_P \vec{g}, \quad (1)$$

$$m_P \frac{dh_p}{dt} = \dot{Q}_{conv} + \dot{Q}_{rad} + \xi \dot{Q}_{gasif} = hA_p(T_g - T_p) + \epsilon\sigma A_p\left(\frac{G}{4\sigma} - T_p^4\right) + \xi \dot{Q}_{gasif}, \quad (2)$$

$$m_P \frac{dY_{p,i}}{dt} = \dot{M}_{gasif,i}. \quad (3)$$

Here, A_p, m_p, $\vec{u_p}$, t, F_g, and F_d are the coal/char particle surface area, its mass, its velocity, the time, and the gravitational and drag momentum source terms. h_p, $\dot{Q}_{conv}$, $\dot{Q}_{rad}$, $\dot{Q}_{gasif}$, ξ, σ, G, and T_p denote the particle enthalpy, the source terms for heat transfer (convective and radiative), the energy source due to gasification, the heat retention coefficient, the Boltzmann constant, the incident radiation, and the particle surface temperature. The heat retention coefficient quantifies the fraction of the gasification heat, which ends up in the solid particle and is assumed to be 0.3 in this work.[45,46] The species conservation equation for the coal particles ($Y_{p,i}$) features source terms for drying, devolatilization, gasification, and oxidation. All source terms, except the one for gasification ($\dot{M}_{gasif,i}$), are zero for the current application. Shrinking particle conversion is assumed for the char particles for simplicity.

The Schiller–Naumann drag correlation is employed for the gas-particle drag,[47]

$$c_D(Re) = \begin{cases} \frac{24}{Re} + \frac{1}{6Re^{1/3}} & \text{if } Re \le 1000 \\ 0.424 & \text{if } Re > 1000. \end{cases} \quad (4)$$

The Ranz–Marshall correlation determines the heat transfer coefficient for the convective heat transfer between coal/char particles and the fluid phase,[48]

$$h = \frac{\left(2 + 0.6Re^{1/2}Pr^{1/3}\right)\kappa_g}{d_p}, \quad (5)$$

where κ_g is the thermal conductivity of the gas phase. The Stefan flow has been neglected in this analysis, since the radiative heat flux

is dominant for the experimental conditions[49] and the particle reaction model did not account for diffusional resistance in the boundary layer. An apparent kinetic model was used to determine the coal char gasification rate ($R_{CO_2,eff}$),

$$R_{CO_2,eff} = A \exp\left(\frac{-E_a}{RT_p}\right) p^n_{CO_2}. \quad (6)$$

Here, R and p_{CO_2} denote the ideal gas constant and the bulk CO_2 partial pressure. The kinetic parameters were taken from the study of Gonzalo-Tirado *et al.*,[50] since they were determined for similar gasification conditions of a similar sub-bituminous coal. The pre-exponential factor (A) is 7.55 kg m^{-2} s^{-1} Pa$^{-0.45}$, the activation energy (E_a) is 148.5 kJ/mol, and the reaction order (n) is 0.45. Initial testing revealed that these kinetic parameters over-predicted the conversion rates. A suitable conversion rate was achieved by reducing A to 1.88 kg/m^{-2} s^{-1} Pa$^{-0.45}$. This nearly fourfold reduction in the reaction rate relative to the Spanish study may be due to actual differences in the reactivities of the different coal chars as well as reflect the lack of accounting for diffusional resistance in the CFD particle reaction model. In addition, it is possible that imperfections in the Spanish reactor flow field and mixing (as reflected in the simulations presented here for the Sandia reactor) could be reflected in the derived kinetic parameters.

Heating rates of individual particles are determined by a backward differentiation scheme using particle temperature (T_i) and residence time (t_i),

$$K_i = \frac{\Delta T_i}{\Delta t_i} = \frac{T_i^{n-1} - T_i^n}{t_i^{n-1} - t_i^n}. \quad (7)$$

Particle burnout (η) is determined by the ash tracer method,[28]

$$\eta_i = \frac{1 - Y_{Ash_0}/Y_{Ash_i}}{1 - Y_{Ash_0}}, \quad (8)$$

where Y_{Ash_0} is the initial ash mass fraction and Y_{Ash_i} is the current or final ash mass fraction. Char burnout would be expected to be overestimated by the simple reaction model employed here near final burnout because the apparent rate expression fails to reproduce impacts due to preferential consumption of more reactive char surfaces[51,52] and high ash concentrations.[52–54]

The coal char's physical and thermo-physical properties are summarized in Table II.

TABLE II. Summary of the coal char's properties.

Property	Quantity
Particle size (d_P)	90 μm–105 μm
Density (ρ_P)	800 kg/m^3
Specific heat capacity (c_p)	1268 J/kg K
Heat of formation (ΔH^0_f)	−5.01 MJ/kg
Emissivity (ϵ)	0.9
Mass fraction of carbon (Y_C)	0.904
Mass fraction of ash (Y_{ash})	0.096

IV. SIMULATION RESULTS

A. 1 atm case

1. Reactor simulation

The steady-state results for the 1 atm case show good agreement with the measured temperatures. Figure 2 compares the simulated and measured reactor and surface temperatures. The surface temperatures ($T_{1,surf}$, $T_{4,surf}$, and $T_{6,surf}$) deviate by up to 22 K, while T_1 is underpredicted by 50 K. The deviations in the predicted temperatures from the measurements at the junction of the two reactor arms and at the outer surface of the pressure vessel may be due to buoyancy effects combined with small gaps between refractory layers, steel pipe, and SiC reactor tube that had to be neglected in the CFD simulation. This could lead to creeping flows leading to heat accumulation in the upper reactor region that are neglected in the simulation. However, since the temperature mid-way down the reactor tube is accurately specified, the temperature distribution in the reactive zone should be similar to the experimental one.

Figure 3 shows the radially averaged mean temperature profile along the axial reactor direction. The char injection point is located

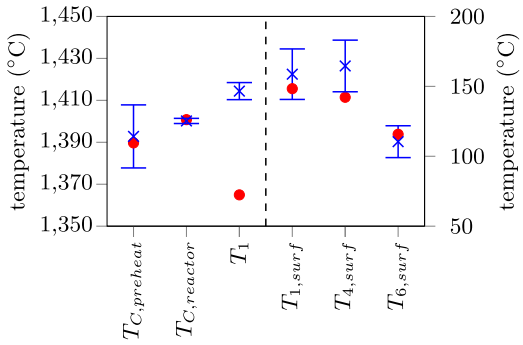

FIG. 2. Comparison of the predicted (dots) and measured (crosses and whiskers for the standard deviation) reactor temperatures for the 1 atm case.

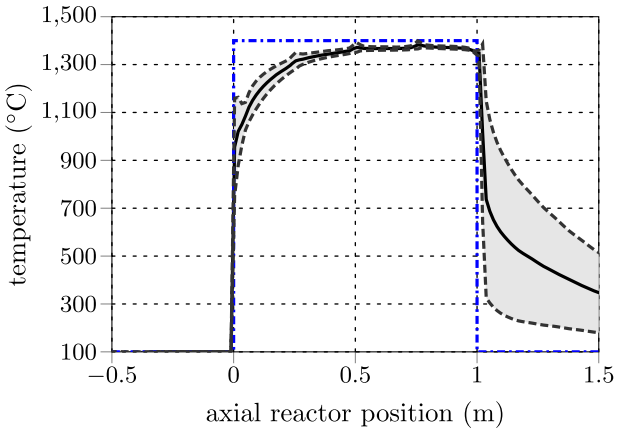

FIG. 3. Simulated gas phase temperatures (solid) and standard deviation of the simulated temperature in the cross section (dashed) and the uniform temperature assumption (dotted-dashed) along the axial reactor direction for the 1 atm case. Char injection is located at 0 m, and the probe is located at 1 m.

at the axial position 0 m toward the upstream direction, while the injection lance extends 0.5 m toward the upstream direction. The reaction zone extends 1 m downstream of the injection point, where the sampling probe and quench are located. The diagram reveals an axial, mean temperature difference of around 250 K along the reaction zone. The radial temperature distribution is represented by the standard deviation and shows minor variations, except in the vicinity of the injection point. The peaks of the standard deviation further downstream are located at the sampling ports located along the reactor whose features increase the turbulence and mixing. The reaction zone fails to reach the target temperature of 1400 °C by ~40 K.

Figure 4 shows the axial velocity contours for the x (parallel to the preheat sidearm) and y (perpendicular to the preheat sidearm) planes in the vicinity of the char injection point. The cross section reduction due to the flow-straightener causes high velocities near the walls and peak velocities at the injection plane. Since the particle carrier gas velocity is much lower than that of the co-flow, a rotating vortex ring is formed. Figure 5 highlights the flow field characteristics with glyphs. In addition to the large vortex effects throughout the flow field, small secondary vortices are revealed next to the lance and the flow-straightener. An asymmetry in the flow field in the x plane is caused by the momentum of the main gases that are flowing horizontally before entering the co-flow inlet. Cross-sectional cuts of velocity through the reaction zone, depicted in Fig. 10, reveal that this is preserved through the reaction zone.

The elevated temperatures in the reactor center, shown in Fig. 6, are caused by the vortex ring. The coal carrier gas is pushed outward toward the walls and mixes with the pre-heated co-flow, causing the colder regions around ±0.02 m radial position. The maximum temperature within the first 0.1 m downstream of the injection point is below 1300 °C, which is more than 100 K below the set point temperature of 1400 °C. The cross-sectional cuts in Fig. 7

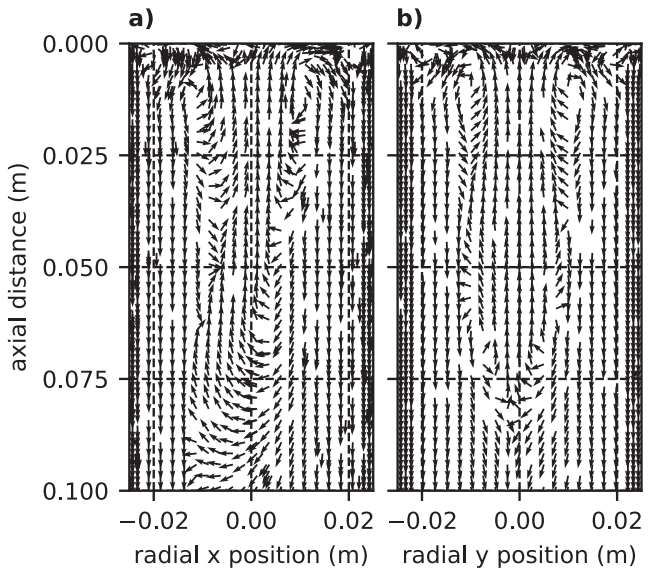

FIG. 5. Velocity field at the x (a) and y (b) planes through the reaction zone in the vicinity of the injection point for the 1 atm case.

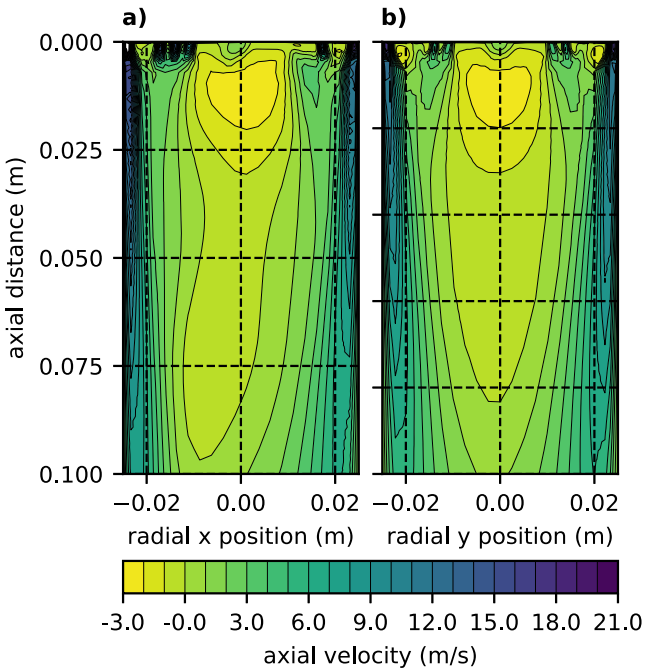

FIG. 4. Axial velocity contours along the x (a) and y (b) planes through the reaction zone in the vicinity of the injection point for the 1 atm case.

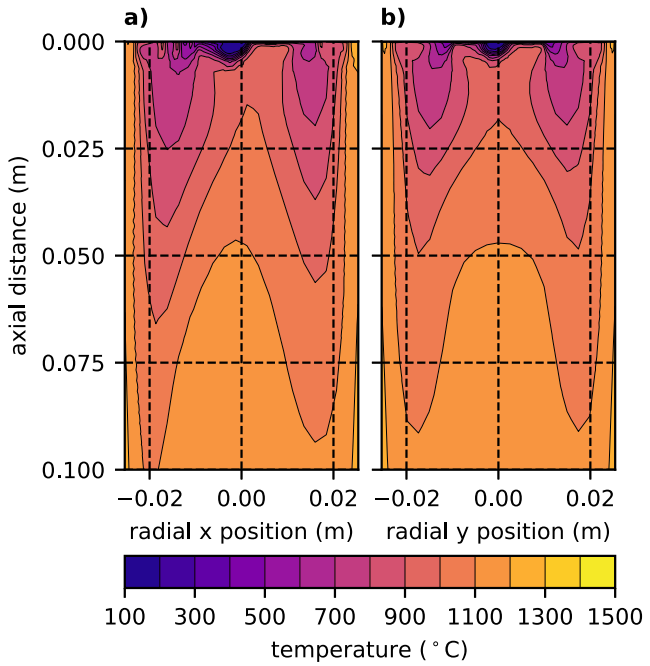

FIG. 6. Temperature contours along the x (a) and y (b) planes through the reaction zone in the vicinity of the injection point for the 1 atm case.

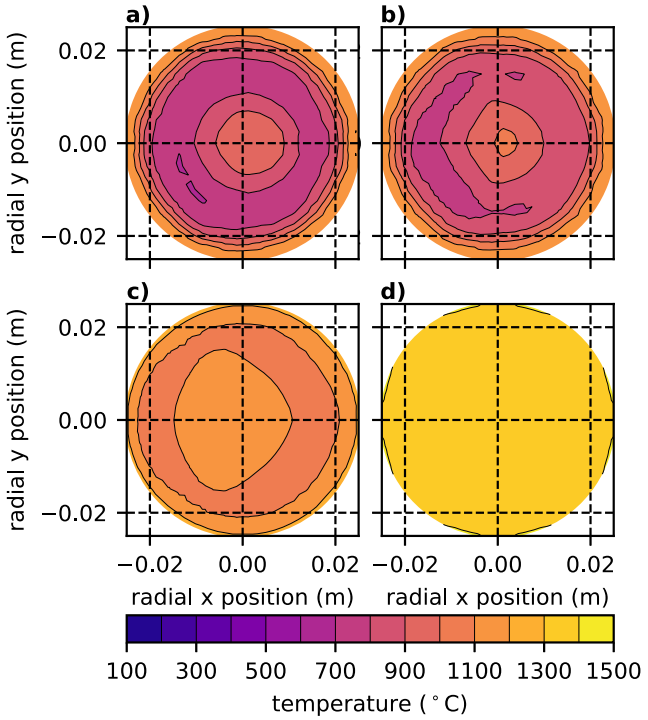

FIG. 7. Temperature contours for reaction zone cross sections along the axial reactor direction for the 1 atm case. Axial positions: (a) 0.01 m; (b) 0.02 m; (c) 0.08 m; (d) 0.50 m.

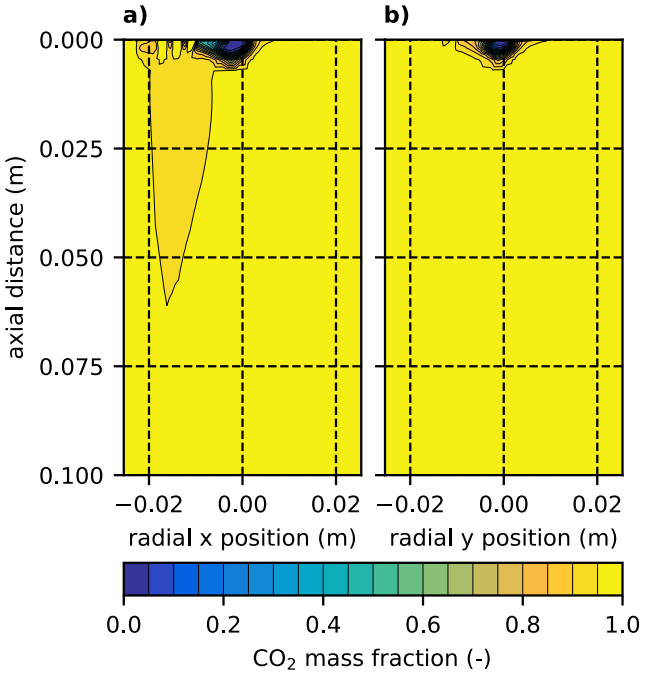

FIG. 8. CO_2 contours along the x (a) and y (b) planes through the reaction zone in the vicinity of the injection point for the 1 atm case.

highlight the temperature stratification near the particle injection point. A uniform temperature field is first approached 0.08 m downstream from the particle injection point.

Figure 8 shows the radial CO_2 contours of the 1 atm case. The CO_2 co-flow mixes within 0.01 m with the N_2 carrier gas. Despite the flow-straightener, the contours on the x plane show an asymmetry due to the flow field.

2. Char gasification simulation

Figure 9 shows the particle temperatures for the simulated and uniform gas phase temperature distributions along the axial reactor direction for the same velocity field. Both cases feature a rapid heat-up when leaving the injection lance. In the case of the hypothetical uniform temperature field, particles reach the expected gasification temperature immediately after entering the reactive zone.

The overall experimentally measured burnout ratio for the 1 atm experiments was **49**%. The mean particle burnout is **51**% for the simulated temperature distribution and **69**% for the uniform temperature distribution. The median residence time of the modeled particles is 0.28 s, while the experimental residence time was estimated to be 0.20 s, based on an assumption of plug flow in the reactor. The average particle heating rates for the simulated and uniform temperature profiles are 50 000 K/s and 60 000 K/s.

Figure 10 indicates char particle positions in the reactor. This indicates that the vortex ring at the exit of the lance disperses the char particles toward the wall, where they tend to stay in the cooler gas regions. The zig-zag-like pattern of the particle positions is caused by the flow characteristics of the flow-straightener. Further downstream, the zig-zag pattern vanishes and the particles distribute over a large part of the cross section. The asymmetry in the particle positions further downstream is caused by the asymmetry in the flow field.

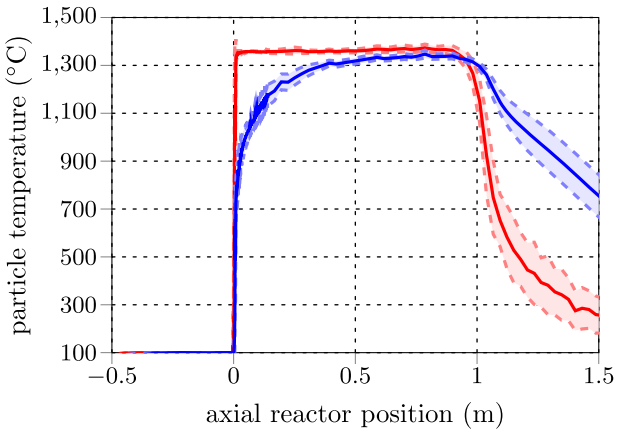

FIG. 9. Particle temperatures (solid) and standard deviation (dashed) for the real (blue) and ideal (red) gas phase temperature distributions along the axial reactor direction for the 1 atm case. Char injection is located at 0 m, and the probe is located at 1 m.

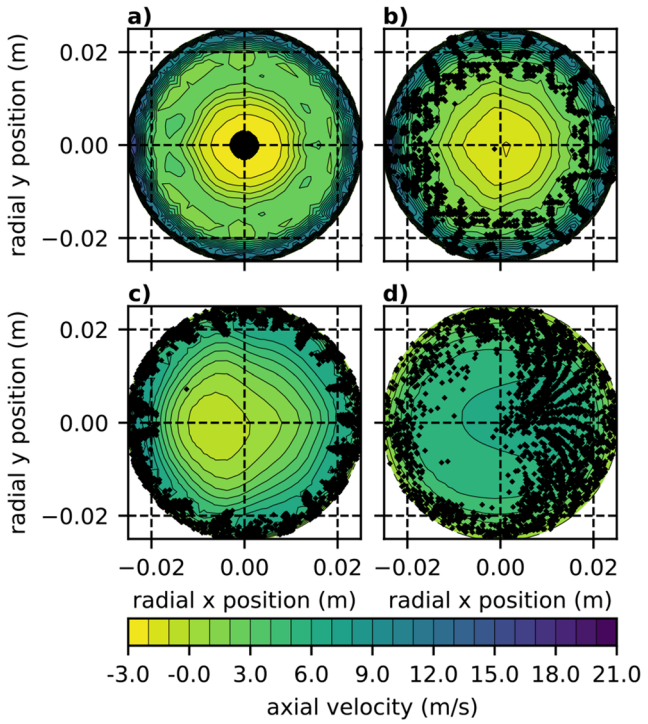

FIG. 10. Axial velocity contours for reaction zone cross sections along the axial reactor direction for the 1 atm case. The symbols indicate intersections of the particle trajectories with the cross-sectional plane [the majority of particles in (b) and (c) are moving upward]. Axial positions: (a) 0.01 m; (b) 0.02 m; (c) 0.08 m; (d) 0.50 m.

B. 8 atm case

1. Reactor simulation

Figure 11 compares the measured and simulated reactor temperatures and surface temperatures for the 8 atm case. As with the 1 atm case, differences for the controlling temperature sensors are negligible, but simulated and experimental surface temperatures ($T_{1,surf}$, $T_{4,surf}$, and $T_{6,surf}$) differ by up to 25 K. T_1 is significantly underpredicted, since heat accumulation in the upper reactor region due to buoyancy induced creeping flows is not captured by the simulation, similar to the 1 atm case. As before, the correct modeling of the preheater and reactor tube temperatures should guarantee that gas temperatures are fairly accurately modeled.

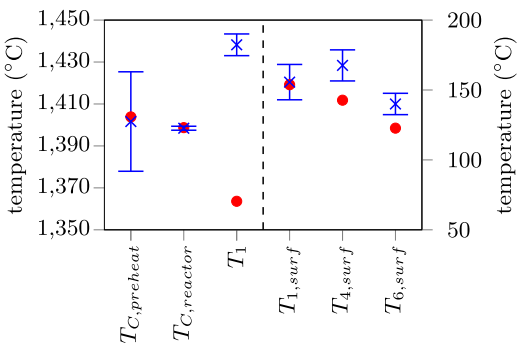

FIG. 11. Comparison of the predicted (dots) and measured (crosses and whiskers for the standard deviation) reactor temperatures for the 8 atm case.

The axial temperature profile, shown in Fig. 12, reveals that the temperature differences and the inequalities in the radial direction are similar as for the 1 atm case. In particular, the mean temperature fails to reach the set point temperature of 1400 °C by ~50 K. Furthermore, an axial temperature difference in the reaction zone of ~250 K exists.

Figure 13 depicts the axial velocity contours for the 8 atm case. Lower velocities occur compared to those in the 1 atm case due to the higher static pressure and the fact that the same mass flow rates for the carrier gas and co-flow are employed at both pressures. Figure 14 reveals a smaller vortex ring than that in the 1 atm case. This is due to a lower relative velocity between the carrier gas and the co-flow in the 8 atm case. However, small vortices exist next to the flow-straightener wall and the injection lance. A flow asymmetry caused by the horizontal co-flow is clearly visible in the x planes of Figs. 13 and 14. Cross-sectional cuts through the reaction zone (Fig. 19) confirm the asymmetric flow profile.

The temperature contours in Fig. 15 feature different characteristics for the 8 atm case than for the 1 atm case (Fig. 6). A homogeneous temperature field exists after ~0.025 m, due to the smaller vortex ring and lower velocities. Figure 16 confirms this. The temperature reaches ~1200 °C within 0.08 m. The x plane temperature contours show no influence of the one-sided co-flow inlet.

The CO_2 contours of the 8 atm case, shown in Fig. 17, reveal an influence of the co-flow on the mixing of the carrier gas and co-flow. An N_2-rich stream penetrates the reactive zone ~0.075 m. The zone where the carrier gas and co-flow mix is smaller than that in the 1 atm case, presumably due to the lower mean axial velocities.

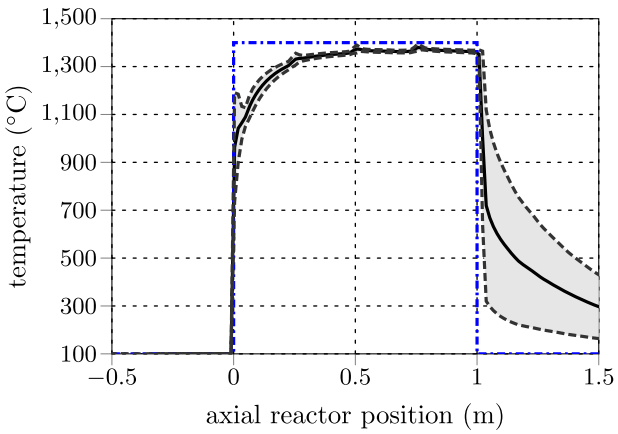

FIG. 12. Simulated gas phase temperatures (solid) and standard deviation of the simulated temperature in the cross section (dashed) and the uniform temperature (dotted-dashed) along the axial reactor direction for the 8 atm case. Char injection is located at 0 m, and the probe is located at 1 m.

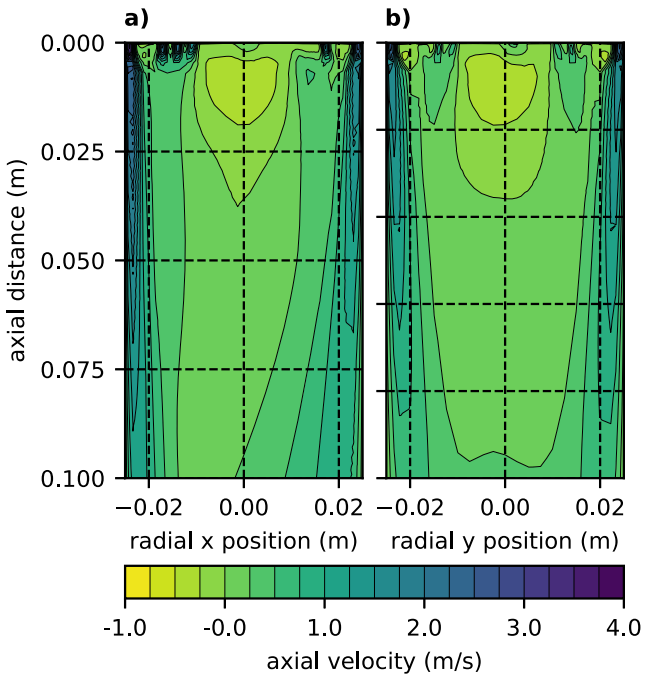

FIG. 13. Axial velocity contours along the x (a) and y (b) planes through the reaction zone in the vicinity of the injection point for the 8 atm case.

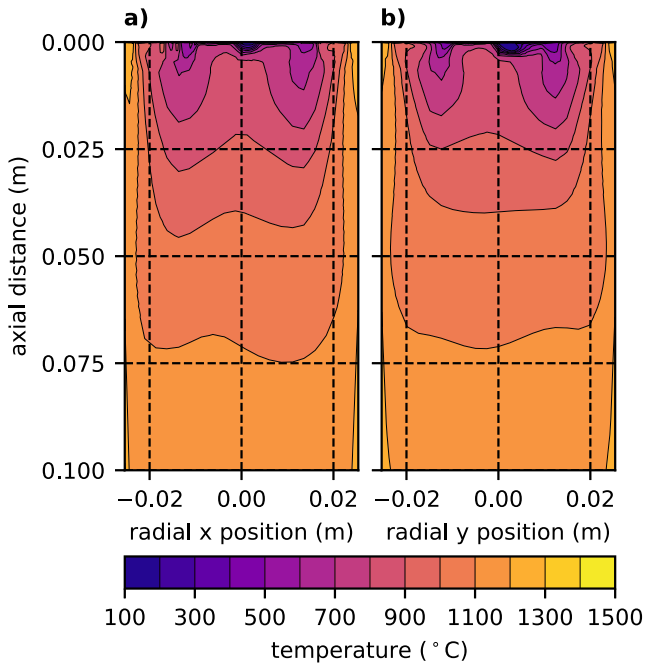

FIG. 15. Temperature contours along the x (a) and y (b) planes through the reaction zone in the vicinity of the injection point for the 8 atm case.

2. Char gasification simulation

Figure 18 shows the mean axial particle temperature profile for the 8 atm case featuring different temperature fields but the same velocity field. The heating rates are similar to those of the 1 atm

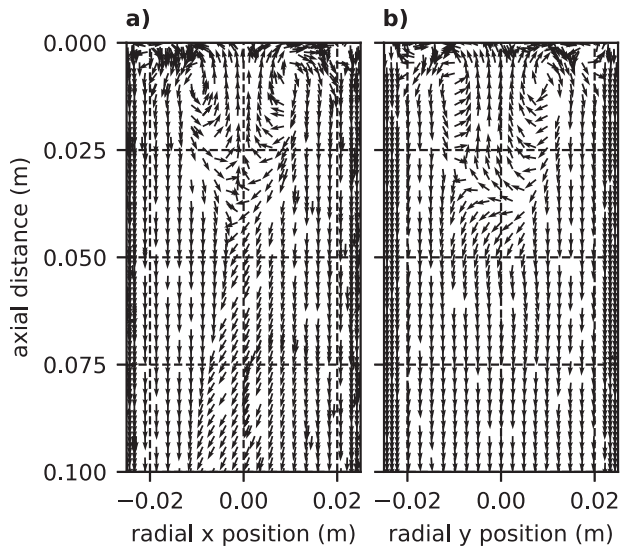

FIG. 14. Velocity field at the x (a) and y (b) planes through the reaction zone in the vicinity of the injection point for the 8 atm case.

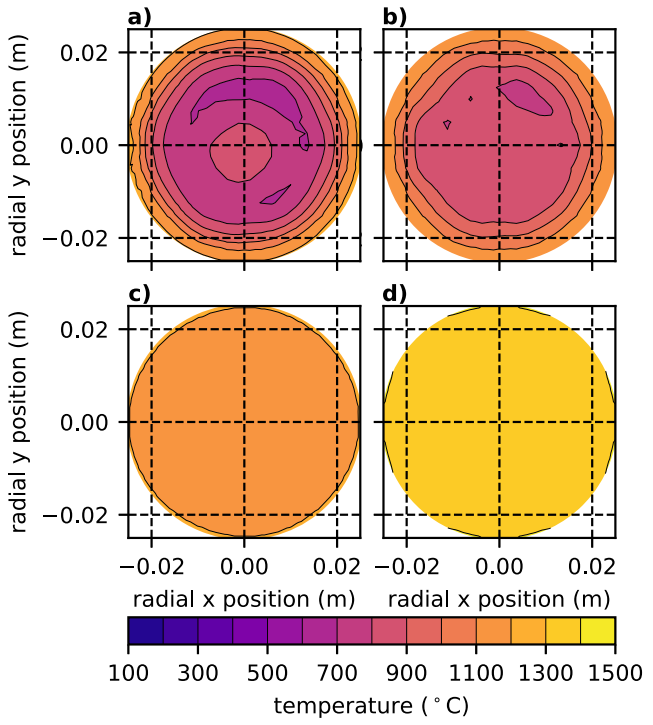

FIG. 16. Temperature contours for reaction zone cross sections along the axial reactor direction for the 8 atm case. Axial positions: (a) 0.01 m; (b) 0.02 m; (c) 0.08 m; (d) 0.50 m.

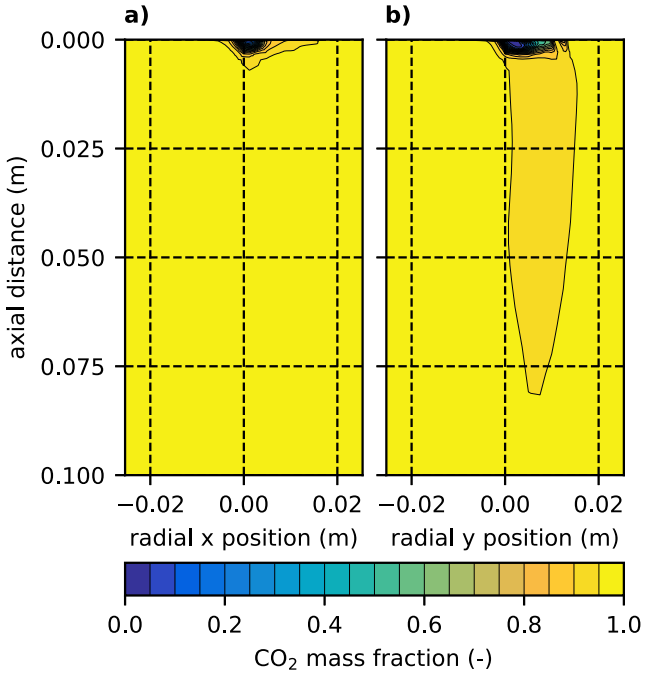

FIG. 17. CO_2 contours along the x (a) and y (b) planes through the reaction zone in the vicinity of the injection point for the 8 atm case.

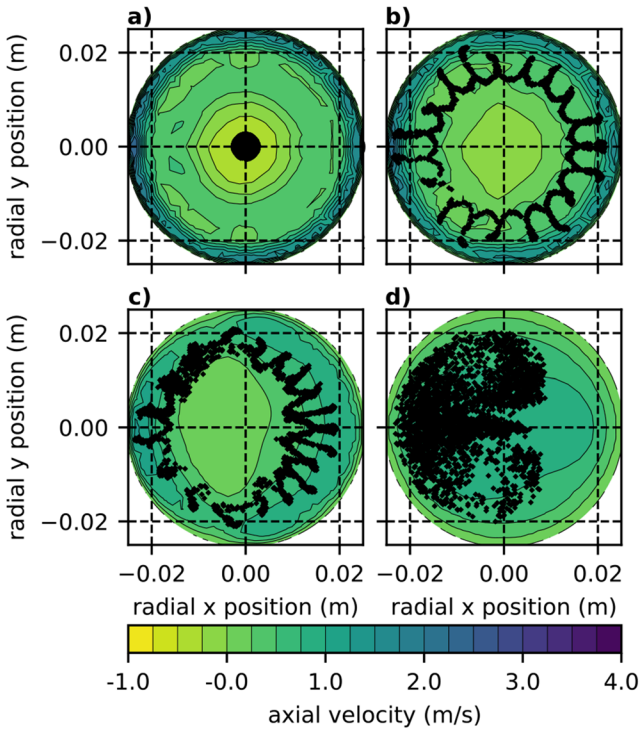

FIG. 19. Axial velocity contours for reaction zone cross sections along the axial reactor direction for the 8 atm case. The symbols indicate intersections of the particle trajectories with the cross-sectional plane [the majority of particles in (b) and (c) are moving upward]. Axial positions: (a) 0.01 m; (b) 0.02 m; (c) 0.08 m; (d) 0.50 m.

case for the simulated temperature distribution. The ideal temperature case shows slower particle heat-up than that of the 1 atm case. The differences in the simulated particle temperatures at the two pressures are caused by a combination of longer residence time of the particles and higher gasification rates for the 8 atm case. The overall experimental burnout ratio for the 8 atm experiments was **100**%. The particle burnout for both temperature distributions is **100**%, since the char particles are fully gasified before leaving the reaction zone. The median residence time of the modeled particles is 1.43 s, while the experimental residence time was estimated to be 1.53 s, based on an assumption of plug flow in the reactor. The average particle heating rates for the simulated and uniform temperature profiles are 20 000 K/s and 80 000 K/s. The significant lower heating rate of the simulated temperatures is a result of lower temperatures prevailing next to the flow-straightener.

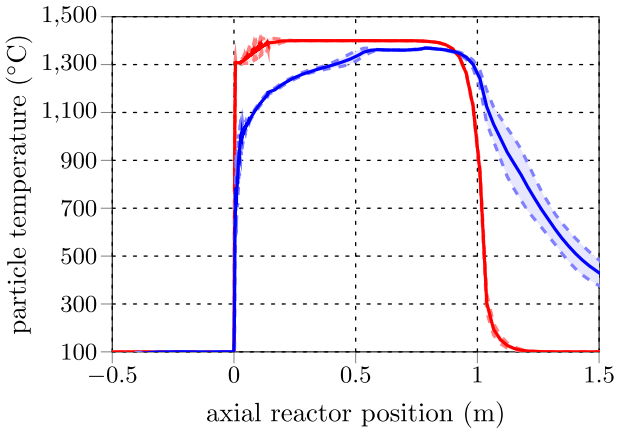

FIG. 18. Particle temperatures (solid) and standard deviation (dashed) for the real (blue) and ideal (red) gas phase temperature distributions along the axial reactor direction for the 8 atm case. Char injection is located at 0 m, and the probe is located at 1 m.

Particles disperse in the 8 atm case due to the vortex at the injection point. The zig-zag pattern in the particle distribution caused by the flow-straightener is also present for the lower velocities of the 8 atm case. Figures 19 and 16 reveal that the particles are enclosed by the cooler gas region in which the carrier gas and co-flow mix in the vicinity of the flow-straightener. In contrast to the 1 atm case, this is a concentric region in the reactor center. The asymmetries in temperature and flow fields are also visible in the cross-sectional cuts for the 8 atm case.

V. SUMMARY AND DISCUSSION

Sandia's pressurized entrained flow reactor (PEFR) has been modeled with CFD. The simulation results are in good agreement with the measured temperatures at the reactor tube surface and pressure vessel surface. Geometric simplifications necessary for the

simulation are probably responsible for minor temperature deviations between experiments and the simulations in the upper reactor region. The simulated temperature distribution of the reaction zone differs substantially from the idealized temperature frequently invoked by experimental researchers, particularly in the mixing zone between the cool injected particles and carrier gas and the surrounding hot reaction gas. The maximum temperature in the simulated reaction zone is ~1350 °C for a nominal reactor set-point temperature of 1400 °C. Moreover, the simulation results indicate that the introduced coal particles continue to reside in the cool carrier gas flow paths for some time after entering the reactor.

The simple, uncoupled modeling approach for char conversion shows reasonable agreement for the overall burnout ratios. These simulations used kinetic parameters with the pre-exponential factor reduced by a factor of 4 from a conventional reactor analysis. In a conventional analysis, the residence time is estimated by assuming plug flow and the temperature is assumed to be the set-point temperature. The reasonably small differences in kinetic rate parameters for a conventional analysis and the analysis in this work are due to the fortuitous offsetting of errors associated with overestimating particle reaction temperatures and underestimating particle residence time in a conventional analysis.

Simulated median particle residence times differ by ~40% for the 1 atm case and ~10% for the 8 atm case compared to those resulting from the plug flow velocities used in experimental analysis. The Stokes number for the particles gives values below unity; thus, the particles follow the flow ideally. The particle residence time is affected by the vortex rings that form at the exit of the flow-straightener and the cross-sectional flow profile featuring higher velocities of the core flow. The two effects counter to each other, as the vortex ring increases the residence time, while the higher velocity decreases the residence time compared to the residence time assuming plug flow. Comparing the 1 atm and 8 atm cases indicates that the vortex size has a significant impact on the particle residence time. The effect of the vortex ring on the residence time dominates in the 1 atm case, while the high core flow velocity dominates in the 8 atm case.

In the 8 atm case, the simulated char particles are fully gasified before leaving the reactor. Therefore, an evaluation of the influence of the temperature in the reaction zone (simulated or uniform) is only possible for the 1 atm case. Approximately 20% more char mass is gasified if a uniform temperature exists in the reactive zone. The relative error of the burnout ratio between simulated and uniform temperatures is 40%. Taking into account the residence time based on the plug flow velocity and the simulated one, the error introduced by the residence time is of the same order of magnitude.

The error introduced to kinetic parameters fitted from experimental burnout and idealized temperature has been estimated by extracting the pre-exponential factors from the 1 atm simulation data and the idealized temperature profile and estimated residence time. The activation energy and reaction order were assumed to be fixed for this calculation. The results indicate an ~10% lower pre-exponential factor for the simulated case.

VI. CONCLUSION

In conclusion, extracting accurate conversion rates and kinetic parameters requires comprehensive models, which incorporate all relevant effects,[15] e.g., temperature gradients and velocity profiles. We strongly recommend that one employs thorough reactor monitoring systems and/or spatially resolved modeling to investigate similar effects for any reactor prior to model fitting of experimental results. These results also highlight the value in employing techniques for determining particle reaction rates through measurements of particle temperature differences from the surrounding flow and assessment of the instantaneous energy balance,[1,4] as such an approach is insensitive to the flow history effects outlined here.

ACKNOWLEDGMENTS

The authors gratefully acknowledge the funding support of K1-MET GmbH, a metallurgical competence center. The research program of the competence center K1-MET is supported by COMET (Competence Center for Excellent Technologies), the Austrian program for competence centers. COMET is funded by the Federal Ministry for Transport, Innovation and Technology, the Federal Ministry for Digital and Economic Affairs, and the province of Upper Austria, Tyrol, and Styria.

Apart from funding, the project activities are financed by the industrial partners Primetals Technologies Austria, voestalpine Stahl, and voestalpine Stahl Donawitz.

Sandia National Laboratories is a multimission laboratory managed and operated by National Technology and Engineering Solutions of Sandia, LLC., a wholly owned subsidiary of Honeywell International, Inc., for the U.S. Department of Energy's National Nuclear Security Administration under Contract No. DE-NA-0003525. The views expressed in this article do not necessarily represent the views of the U.S. Department of Energy or the United States government.

APPENDIX A: INSULATION MATERIAL TESTS

A cylindrical test vessel was constructed to examine the thermal conductivity behavior of porous refractory insulation at elevated pressures. The vessel has a central heated test section, with a length of 0.3 m and a diameter of 0.3 m for the refractory insulation. Concentric insulation layers enclose the electrical heating element in the center, which is separated from the first layer of insulation by argon gas. Thermocouples were embedded in the insulation at various radial positions along the axis of the vessel. Figure 20 shows

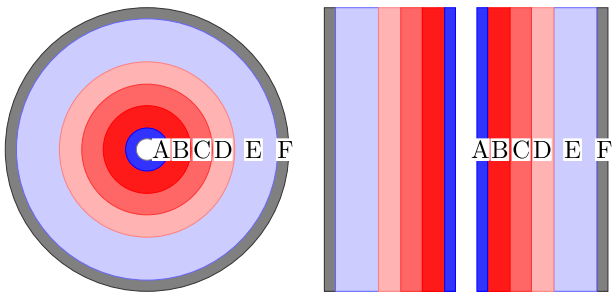

FIG. 20. Schematic top (left) and side (right) views of the insulation test simulation domain. A: argon zone; B: AL30 layer; C: inner ALC layer; D: outer ALC layer; E: AXL layer; F: SST 316 jacket.

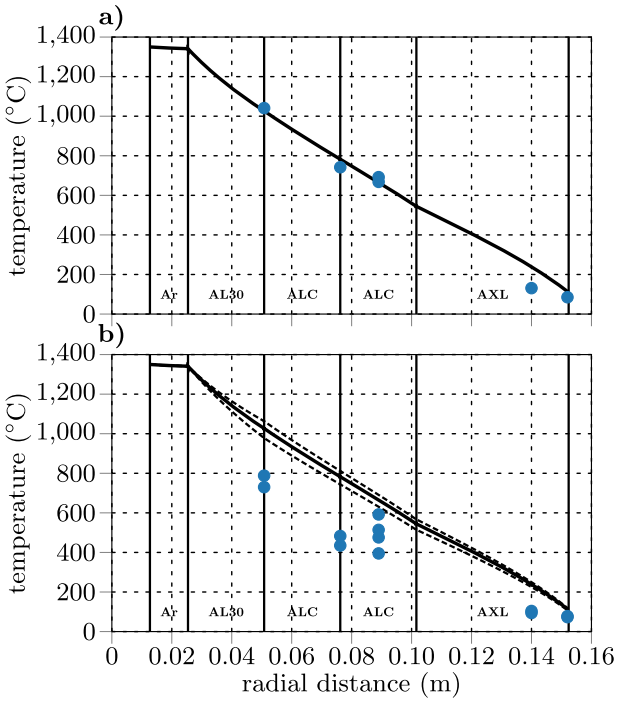

FIG. 21. Comparison of experimental temperatures and simulation results for the 1 atm (a) and 20 atm (b) vertical test cases. Dashed lines show the results for ±20% AL30 thermal conductivity.

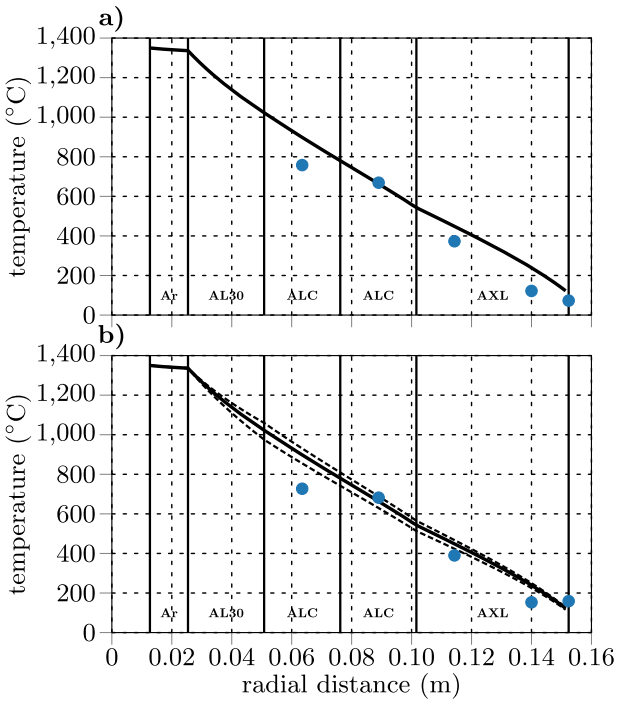

FIG. 22. Comparison of experimental temperatures and simulation results for the 1 atm (a) and 20 atm (b) horizontal test cases. Dashed lines show the results for ±20% AL30 thermal conductivity.

the radial and axial cuts through the test section to illustrate the setup. The heating element is not shown. The vessel was mounted on a stand that allowed it to be supported in either a vertical or a horizontal arrangement, to allow for an investigation of buoyancy effects. Tests at ambient pressures and at 20 atm were conducted. Heat flux analysis was performed using steady-state temperature measurements. The evaluations indicate a heat loss of ~350 W for the test section and a heater surface temperature of ~1350 °C.

Again, we used *chtMultiRegionFoam* for the insulation simulations. Boundary conditions were fixed temperature at the inner boundary (1350 °C), while a natural convection boundary condition according to Tetsu and Haruo[55] was set at the vessel surface.

TABLE III. Thermo-physical properties of refractory materials.

AL30[65,66]			
Density	c_1	480	kg/m^3
Specific heat capacity	c_1	1047	J/kg/K
Thermal conductivity	c_1	1.97×10^{-2}	W/m/K
	c_2	1.29×10^{-4}	
ALC[67]			
Density	c_1	240	kg/m^3
Specific heat capacity	c_1	1024	J/kg/K
Thermal conductivity	c_1	-5.25×10^{-2}	W/m/K
	c_2	1.77×10^{-4}	
ASH[68]			
Density	c_1	320	kg/m^3
Specific heat capacity	c_1	1032	J/kg/K
Thermal conductivity	c_1	-2.74×10^{-2}	W/m/K
	c_2	1.61×10^{-4}	
AXL[69]			
Density	c_1	280	kg/m^3
Specific heat capacity	c_1	1024	J/kg/K
Thermal conductivity	c_1	-1.51×10^{-2}	W/m/K
	c_2	1.72×10^{-4}	
Contronics 3000F[70]			
Density	c_1	192	kg/m^3
Specific heat capacity	c_1	1046.7	J/kg/K
Thermal conductivity	c_1	-3.96×10^{-2}	W/m/K
	c_2	1.63×10^{-4}	

TABLE IV. Thermo-physical properties of ceramic materials.

Al_2O_3[71,72]								
Density		3950	kg/m^3					
Specific heat capacity[72]	c_1	c_2	c_3	c_4	c_5	c_6	c_7	c_8
J/kg/K	−627.99	9.09	-2.12×10^{-2}	2.79×10^{-5}	-2.16×10^{-8}	9.74×10^{-12}	-2.37×10^{-15}	2.41×10^{-19}
Thermal conductivity[71]	c_1	c_2	c_3	c_4	c_5	c_6	c_7	c_8
W/m/K	106.04	−0.45	9.69×10^{-4}	-1.22×10^{-6}	9.14×10^{-10}	-4.05×10^{-13}	9.73×10^{-17}	-9.79×10^{-21}
SiC[73,74]								
Density		3950	kg/m^3					
Specific heat capacity[74]	c_1	c_2	c_3	c_4	c_5	c_6	c_7	c_8
J/kg/K	−1141.26	6.52	-8.99×10^{-3}	7.80×10^{-6}	-4.40×10^{-9}	1.57×10^{-12}	-3.24×10^{-16}	2.90×10^{-20}
Thermal conductivity[74]	c_1	c_2	c_3	c_4	c_5	c_6	c_7	c_8
W/m/K	114.15	−0.22	3.03×10^{-4}	-2.96×10^{-7}	1.90×10^{-10}	-7.59×10^{-14}	1.70×10^{-17}	-1.62×10^{-21}

Thermo-physical properties of the refractory materials and the SST 316 jacket were taken from Appendix B. The thermo-physical properties of argon from the GRI3.0 mechanism were employed for the fluid phase at the center. A SIMPLE algorithm advanced the simulations to the steady-state. Residuals for the steady-state were below 10^{-8} for the energy equation and below 10^{-3} for the momentum equation. During the solution process, simulations at 20 atm pressure crashed repeatedly and the velocity and pressure snapshots showed regular vortices in the argon region. Various researchers have investigated the buoyancy driven flow in horizontal concentric cylinder annuli.[56–60] From their results, it is evident that the steady crescent-shaped flow transforms into an unsteady periodically oscillating flow exceeding a critical Rayleigh number. Similar investigations have been performed for vertical concentric cylinder annuli.[61–63] They show that transient effects exist above a critical Rayleigh number. The discrepancies found here between simulations and experiments in the 20 atm case might be caused by these transient effects, since steady-state solvers neglect them. An indication of possible transient effects in steady-state simulations is poor convergence or crashes.

Figures 21 and 22 compare the measured temperatures and simulation steady-state results for the vertical and the horizontal test cases. Simulations show good agreement for the tests at 1 atm. Steel pipe surface temperatures only differ by a few Kelvin between the simulations and the measurements. The horizontal test at 20 atm agrees well with the simulations. The vertical results at 20 atm over-predict the temperature throughout the volume, although the experimental and predicted surface temperatures show good agreement. Transient flow phenomena might be responsible for some of the deviations between experiments and calculations. An alternative explanation is a pressure dependence of the thermal conductivity of the refractory insulation. To test this assumption, the thermal conductivity of AL30 was decreased and increased by 20%. The dashed lines indicate the results using the lower and higher AL30 conductivities. Both variations are too low to significantly alter the simulation results. Thus, the transient flow effects seem to be a better rationale for the deviations between experimental and simulation results, particularly since the measured and predicted temperatures are in good agreement for the 20 atm case when the cylinder is horizontal.

APPENDIX B: MATERIAL PROPERTIES

Temperature dependent properties (ϕ) were expressed as polynomial functions up to seventh order,

$$\phi = c_1 + c_2 T + c_3 T^2 + c_4 T^3 + c_5 T^4 + c_6 T^5 + c_7 T^6 + c_8 T^7. \quad \text{(B1)}$$

For constant properties, only c_1 deviates from zero.

TABLE V. Thermo-physical properties of steel materials.

SST 314[75]			
Density	c_1	7185	kg/m^3
Specific heat capacity	c_1	469.44	J/kg/K
	c_2	0.13	J/kg/K
Thermal conductivity	c_1	8.12	W/m/K
	c_2	1.62×10^{-2}	
SST 316[75]			
Density	c_1	7060	kg/m^3
Specific heat capacity	c_1	458.98	J/kg/K
	c_2	0.13	J/kg/K
Thermal conductivity	c_1	9.25	W/m/K
	c_2	1.57×10^{-2}	

TABLE VI. Mean emissivity coefficients.

Material	Value	
Al_2O_3	0.75	Estimated[72,76]
AL30	0.45	Estimated[76,77]
ALC	0.45	Estimated[76,77]
ASH	0.45	Estimated[76,77]
AXL	0.45	Estimated[76,77]
Contronics 3000F	0.45	Estimated[76,77]
SiC	0.75	Estimated[78,79]
SST 314	0.40	Estimated[80]
SST 316	0.40	Estimated[80]

Tables III–V summarize the employed polynomial expressions for the thermo-physical properties of the refractory materials, the ceramic parts, and the steel parts.

Table VI summarizes the employed mean emission coefficients ϵ. They were estimated based on mean emissivity measurements, spectral measurements, and subsequent interpolation of the black body function[64] and interpolation between pure substance values, e.g., for SiC.

DATA AVAILABILITY

The data that support the findings of this study are available from the corresponding author upon reasonable request.

REFERENCES

[1] R. E. Mitchell, "Experimentally determined overall burning rates of coal chars," Combust. Sci. Technol. **53**, 165–186 (1987).

[2] K. A. Davis, R. H. Hurt, N. Y. C. Yang, and T. J. Headley, "Evolution of char chemistry, crystallinity, and ultrafine structure during pulverized-coal combustion," Combust. Flame **100**, 31–40 (1995).

[3] M. J. Wornat, R. H. Hurt, N. Y. C. Yang, and T. J. Headley, "Structural and compositional transformations of biomass chars during combustion," Combust. Flame **100**, 131–143 (1995).

[4] J. J. Murphy and C. R. Shaddix, "Combustion kinetics of coal chars in oxygen-enriched environments," Combust. Flame **144**, 710–729 (2006).

[5] C. R. Shaddix and A. Molina, "Particle imaging of ignition and devolatilization of pulverized coal during oxy-fuel combustion," Proc. Combust. Inst. **32**, 2091–2098 (2009).

[6] Y. Liu, M. Geier, A. Molina, and C. R. Shaddix, "Pulverized coal stream ignition delay under conventional and oxy-fuel combustion conditions," Int. J. Greenhouse Gas Control **5**, S36–S46 (2011), part of special issue: Oxyfuel Combustion Technology—Working Toward Demonstration and Commercialisation.

[7] M. Geier, C. R. Shaddix, K. A. Davis, and H.-S. Shim, "On the use of single-film models to describe the oxy-fuel combustion of pulverized coal char," Appl. Energy **93**, 675–679 (2012), part of special issue: (1) Green Energy; (2) Special Section from papers presented at the 2nd International Energy 2030 Conference.

[8] D. Kim, S. Choi, C. R. Shaddix, and M. Geier, "Effect of Co_2 gasification reaction on char particle combustion in oxy-fuel conditions," Fuel **120**, 130–140 (2014).

[9] T. Li, Y. Niu, L. Wang, C. Shaddix, and T. Løvås, "High temperature gasification of high heating-rate chars using a flat-flame reactor," Appl. Energy **227**, 100–107 (2018), part of special issue: Transformative Innovations for a Sustainable Future—Part III.

[10] N. M. Laurendeau, "Heterogeneous kinetics of coal char gasification and combustion," Prog. Energy Combust. Sci. **4**, 221–270 (1978).

[11] R. H. Hurt and R. E. Mitchell, "Unified high-temperature char combustion kinetics for a suite of coals of various rank," Symp. (Int.) Combust. **24**, 1243–1250 (1992), part of special issue: Twenty-Fourth Symposium on Combustion.

[12] R. H. Hurt and R. E. Mitchell, "On the combustion kinetics of heterogeneous char particle populations," Symp. (Int.) Combust. **24**, 1233–1241 (1992), part of special issue: Twenty-Fourth Symposium on Combustion.

[13] R. E. Mitchell, "An intrinsic kinetics-based, particle-population balance model for char oxidation during pulverized coal combustion," Proc. Combust. Inst. **28**, 2261–2270 (2000).

[14] L. Liu, Y. Cao, Q. Liu, and J. Yang, "Experimental and kinetic studies of coal–Co_2 gasification in isothermal and pressurized conditions," RSC Adv. **7**, 2193–2201 (2017).

[15] D. Chen, Z. Zhang, Z. Li, Z. Lv, and N. Cai, "Optimizing *in-situ* char gasification kinetics in reduction zone of pulverized coal air-staged combustion," Combust. Flame **194**, 52–71 (2018).

[16] A. Mishra, S. Gautam, and T. Sharma, "Effect of operating parameters on coal gasification," Int. J. Coal Sci. Technol. **5**, 113–125 (2018).

[17] V. Raghavan, S. E. Whitney, R. J. Ebmeier, N. V. Padhye, M. Nelson, H. J. Viljoen, and G. Gogos, "Thermal analysis of the vortex tube based thermocycler for fast DNA amplification: Experimental and two-dimensional numerical results," Rev. Sci. Instrum. **77**, 094301 (2006).

[18] R. Lemaire and S. Menanteau, "Development and numerical/experimental characterization of a lab-scale flat flame reactor allowing the analysis of pulverized solid fuel devolatilization and oxidation at high heating rates," Rev. Sci. Instrum. **87**, 015104 (2016).

[19] M. A. Jama, K. Nikiforow, M. S. Qureshi, and V. Alopaeus, "CFD analysis of laboratory scale phase equilibrium cell operation," Rev. Sci. Instrum. **88**, 105110 (2017).

[20] J. Yang, Q. Liu, and W. Dai, "Computational fluid dynamics analysis and experimental study of a low measurement error temperature sensor used in climate observation," Rev. Sci. Instrum. **88**, 024902 (2017).

[21] T. Li, L. Wang, X. Ku, B. M. Güell, T. Løvås, and C. R. Shaddix, "Experimental and modeling study of the effect of torrefaction on the rapid devolatilization of biomass," Energy Fuels **29**, 4328–4338 (2015).

[22] A. L. Brown, D. C. Dayton, M. R. Nimlos, and J. W. Daily, "Design and characterization of an entrained flow reactor for the study of biomass pyrolysis chemistry at high heating rates," Energy Fuels **15**, 1276–1285 (2001).

[23] M. Simone, E. Biagini, C. Galletti, and L. Tognotti, "Evaluation of global biomass devolatilization kinetics in a drop tube reactor with cfd aided experiments," Fuel **88**, 1818–1827 (2009).

[24] C. Meesri and B. Moghtaderi, "Experimental and numerical analysis of sawdust-char combustion reactivity in a drop tube reactor," Combust. Sci. Technol. **175**, 793–823 (2003).

[25] S. Sun, H. Tian, Y. Zhao, R. Sun, and H. Zhou, "Experimental and numerical study of biomass flash pyrolysis in an entrained flow reactor," Bioresour. Technol. **101**, 3678–3684 (2010).

[26] R. J. Flaxman and W. L. H. Hallett, "Flow and particle heating in an entrained flow reactor," Fuel **66**, 607–611 (1987).

[27] C. R. Monson and G. J. Germane, "A high pressure drop-tube facility for coal combustion studies," Energy Fuels **7**, 928–936 (1993).

[28] N. Gat, L. M. Cohen, A. B. Witte, and R. M. Denison, "Ash loss and the "seeded-tracer" technique for the determination of mass balance in rapid heating coal pyrolysis experiments," Combust. Flame **57**, 255–263 (1984).

[29] R. J. Anderson, R. G. Logan, C. T. Meyer, and R. A. Dennis, "A combustion/deposition entrained reactor for high-temperature/pressure studies of coal and coal minerals," Rev. Sci. Instrum. **61**, 1294–1302 (1990).

[30] C. W. Lee, A. W. Scaroni, and R. G. Jenkins, "Effect of pressure on the devolatilization and swelling behaviour of a softening coal during rapid heating," Fuel **70**, 957–965 (1991).

[31] M. J. Aho, K. M. Paakkinen, P. M. Pirkonen, P. Kilpinen, and M. Hupa, "The effects of pressure, oxygen partial pressure, and temperature on the formation of N_2O, NO, and NO_2 from pulverized coal," Combust. Flame **102**, 387–400 (1995).

[32] K. J. Bateman, G. J. Germane, L. D. Smoot, and C. N. Eatough, "A facility for high-pressure measurement of reaction rates of millimeter-sized coal," Energy Fuels **9**, 295–301 (1995).

[33]L. K. Hansen, J. Fjellerup, P. Stoholm, and M. Kirkegaard, in *The Pressurized Entrained Flow Reactor at Riso: Design Report*, Internal Report No. Risø-R-822(EN) (Risø National Laboratory, 1995).
[34]T. Reichelt, T. Joutsenoja, H. Spliethoff, K. R. G. Hein, and R. Hernberg, "Characterization of burning char particles under pressurized conditions by simultaneous *in situ* measurement of surface temperature and size," Symp. (Int.) Combust. **27**, 2925–2932 (1998).
[35]S. Ouyang, H. Yeasmin, and J. Mathews, "A pressurized drop-tube furnace for coal reactivity studies," Rev. Sci. Instrum. **69**, 3036–3041 (1998).
[36]E. Litovsky, M. Shapiro, and A. Shavit, "Gas pressure and temperature dependences of thermal conductivity of porous ceramic materials: Part 2. Refractories and ceramics with porosity exceeding 30%," J. Am. Ceram. Soc. **79**, 1366–1376 (1996).
[37]K. Daryabeigi, G. R. Cunnington, and J. R. Knutson, "Combined heat transfer in high-porosity high-temperature fibrous insulation: Theory and experimental validation," J. Thermophys. Heat Transfer **25**, 536–546 (2011).
[38]N. P. G. Lumley, E. Ford, E. Minford, and J. M. Porter, "A simplified model for effective thermal conductivity of highly porous ceramic fiber insulation," J. Therm. Sci. Eng. Appl. **7**, 041022 (2015).
[39]G. P. Smith, D. M. Golden, M. Frenklach, N. W. Moriarty, B. Eiteneer, M. Goldenberg, C. T. Bowman, R. K. Hanson, S. Song, W. C. Gardiner, Jr., V. V. Lissianski, and Z. Qin, GRI-Mech 3.0, http://www.me.berkeley.edu/gri_mech/, 2018.
[40]H. G. Weller, G. Tabor, H. Jasak, and C. Fureby, "A tensorial approach to computational continuum mechanics using object-oriented techniques," Comput. Phys. **12**, 620–631 (1998).
[41]P. J. Martínez Ferrer, D. M. Causon, L. Qian, C. G. Mingham, and Z.H. Ma, "A multi-region coupling scheme for compressible and incompressible flow solvers for two-phase flow in a numerical wave tank," Comput. Fluids **125**, 116–129 (2016).
[42]F. Menter, J. C. Ferreira, T. Esch, B. Konno, and A. Germany, "The SST turbulence model with improved wall treatment for heat transfer predictions in gas turbines," in *Proceedings of the International Gas Turbine Congress* (Gas Turbine Society of Japan, 2003), pp. 2–7.
[43]W. L. Grosshandler, "RADCAL: A narrow-band model for radiation—Calculations in a combustion environment," Technical Note 1402, National Institute of Standards and Technology (NIST), Gaithersburg, MD, 1993.
[44]W. Kast, H. Klan, and A. Thess, "F2 heat transfer by free convection: External flows," in *VDI Heat Atlas* (Springer Berlin Heidelberg, Berlin, Heidelberg, 2010), pp. 667–672.
[45]M. C. Reis, F. Alobaid, and Y. Wang, "Toward the modeling of combustion reactions through discrete element method (DEM) simulations," Comput. Part. Mech. **5**, 579–591 (2018).
[46]R. K. Boyd and J. H. Kent, "Three-dimensional furnace computer modelling," Symp. (Int.) Combust. **21**, 265–274 (1988), part of special issue: Twenty-First Symposuim (International on Combustion).
[47]L. Schiller and A. Naumann, "A drag coefficient correlation," Z. Ver. Dtsch. Ing. **77**, 318–320 (1935).
[48]W. E. Ranz, "Friction and transfer coefficients for single particles and packed beds," Chem. Eng. Prog. **48**, 247–253 (1952).
[49]Y. Kuang, B. He, W. Tong, C. Wang, and Z. Ying, "Effects of oxygen concentration and inlet velocity on pulverized coal mild combustion," Energy **198**, 117376 (2020).
[50]C. Gonzalo-Tirado, S. Jiménez, and J. Ballester, "Gasification of a pulverized sub-bituminous coal in CO_2 at atmospheric pressure in an entrained flow reactor," Combust. Flame **159**, 385–395 (2012).
[51]R. H. Hurt, M. M. Lunden, E. G. Brehob, and D. J. Maloney, "Statistical kinetics for pulverized coal combustion," Symp. (Int.) Combust. **26**, 3169–3177 (1996).
[52]R. Hurt, J.-K. Sun, and M. Lunden, "A kinetic model of carbon burnout in pulverized coal combustion," Combust. Flame **113**, 181–197 (1998).
[53]J. J. Murphy and C. R. Shaddix, "Effect of reactivity loss on apparent reaction order of burning char particles," Combust. Flame **157**, 535–539 (2010).
[54]Y. Niu, S. Liu, C. R. Shaddix, and S. Hui, "An intrinsic kinetics model to predict complex ash effects (ash film, dilution, and vaporization) on pulverized coal char burnout in air (O_2/N_2) and oxy-fuel (O_2/CO_2) atmospheres," Proc. Combust. Inst. **37**, 2781–2790 (2019).
[55]F. Tetsu and U. Haruo, "Laminar natural-convective heat transfer from the outer surface of a vertical cylinder," Int. J. Heat Mass Transfer **13**, 607–615 (1970).
[56]R. E. Powe, C. T. Carley, and E. H. Bishop, "Free convective flow patterns in cylindrical annuli," J. Heat Transfer **91**, 310–314 (1969).
[57]L. R. Mack and E. H. Bishop, "Natural convection between horizontal concentric cylinders for low Rayleigh numbers," Q. J. Mech. Appl. Math. **21**, 223–241 (1968).
[58]T. Adachi and S. Imai, "Three-dimensional linear stability of natural convection in horizontal concentric annuli," Int. J. Heat Mass Transfer **50**, 1388–1396 (2007).
[59]T. H. Kuehn and R. J. Goldstein, "An experimental and theoretical study of natural convection in the annulus between horizontal concentric cylinders," J. Fluid Mech. **74**, 695–719 (1976).
[60]R. Yan-Fei, M. Yasutomi, F. Kenji, T. Yasuyuki, and H. Shu, "Flow patterns of natural convection in horizontal cylindrical annuli," Int. J. Heat Mass Transfer **28**, 705–714 (1985).
[61]B. B. Rogers and L. S. Yao, "Natural convection in a heated annulus," Int. J. Heat Mass Transfer **36**, 35–47 (1993).
[62]I. G. Choi and S. A. Korpela, "Stability of the conduction regime of natural convection in a tall vertical annulus," J. Fluid Mech. **99**, 725–738 (1980).
[63]L.-C. Weng and H.-S. Chu, "Combined natural convection and radiation in a vertical annulus," Heat Mass Transfer **31**, 371–379 (1996).
[64]D. Lawson, "The blackbody fraction, infinite series and spreadsheets," Int. J. Eng. Educ. **20**, 984–990 (2004).
[65]Alumina Type AL-30—Technical Data Bulletin, Zirca Ceramics, Inc., 2016.
[66]Alumina Type AL-30AA—Technical Data Bulletin, Zirca Ceramics, Inc., 2016.
[67]Alumina Type ALC-AA—Technical Data Bulletin, Zirca Ceramics, Inc., 2016.
[68]Alumina-Silica Type ASH—Technical Data Bulletin, Zirca Ceramics, Inc., 2016.
[69]Alumina-Silica Type AXL—Technical Data Bulletin, Zirca Ceramics, Inc., 2016.
[70]Ceramic Paper 3000°F—Technical Data Bulletin, Cotronics Corp., 2018.
[71]B. Schulz, "High temperature thermal conductivity of irradiated and non-irradiated α-Al_2O_3," J. Nucl. Mater. **155-157**, 348–351 (1988).
[72]P. Auerkari, *Mechanical and Physical Properties of Engineering Alumina Ceramics* (Technical Research Centre of Finland, Espoo, 1996).
[73]Halsic-R/-RX/-I/-S—Technical Specifications, Haldenwanger—Morgen Advanced Ceramics, 2018.
[74]R. G. Munro, "Material properties of a sintered α-SiC," J. Phys. Chem. Ref. Data **26**, 1195–1203 (1997).
[75]C. S. Kim, "Thermophysical properties of stainless steels," Technical Report No. AN-75-55, Argonne National Laboratory, IL, USA, 1975.
[76]A. H. Sully, E. A. Brandes, and R. B. Waterhouse, "Some measurements of the total emissivity of metals and pure refractory oxides and the variation of emissivity with temperature," Br. J. Appl. Phys. **3**, 97–101 (1952).
[77]J. Hoornstra, M. Turecky, and D. Maatman, "Measurement of radiant properties of ceramic foam," Technical Report No. ECN-RX-94-059, Netherlands Energy Research Foundation (ECN), 1994.
[78]Y. Zhang, J. Dai, X. Lu, and Y. Wu, "Effects of temperature on the spectral emissivity of C/SiC composites," Ceram.-Silik. **60**, 152–155 (2016).
[79]J. E. Stewart and J. C. Richmond, "Infrared emission spectrum of silicon carbide heating elements," J. Res. Natl. Bur. Stand. **59**, 405–409 (1957).
[80]T. Paloposki and L. Liedquist, *Steel Emissivity at High Temperatures* (VTT, 2005).